The Journal of the Astronautical Sciences, Vol. 53, No. 4, October–December 2005, pp. 445–463

The Potential of Remote Sensing for Neutral Atmospheric Density Estimation in a Data Assimilation System

C. F. Minter,[1] T. J. Fuller-Rowell,[2] and M. V. Codrescu[3]

Abstract

New data assimilation techniques have improved time-dependent estimates of the neutral atmospheric density, making it possible to better estimate the drag perturbation on low-Earth-orbiting satellites. This study looks at the potential for using satellite remote sensing from space as an effective density observation source in a data assimilation system. Changes in the neutral density can occur on a minute-to-minute basis, particularly during geomagnetic storms. Although coverage from only a few (two) satellites may be limited, remote sensing provides observations with a high temporal and spatial resolution. To quantify the effectiveness of the observing platform, a simulated "truth" neutral atmosphere is created using a physical model. This "truth" neutral atmosphere is sampled according to the mechanics of the remote sensing platform, and the results are statistically evaluated. With the resolution afforded by remote sensing, results show that two remote sensing satellites provide a stable solution of degree 4 (5×5) every ten minutes. Although coverage from two remote sensing satellites is limited, the coverage is sufficient to provide a pattern correlation coefficient consistently higher than 0.92.

Introduction

Background

After the oblateness of the Earth, atmospheric drag is the next most significant natural perturbation force affecting satellite trajectories for low-Earth-orbiting

[1]Research Associate, The Cooperative Institute for Research in Environmental Sciences, University of Colorado, and the National Oceanic and Atmospheric Administration, Space Environment Center, 325 Broadway, Boulder, CO 80305-3337, USA, email: Clifton.Minter@Colorado.edu.
[2]Senior Research Associate, The Cooperative Institute for Research in Environmental Sciences, University of Colorado, and the National Oceanic and Atmospheric Administration, Space Environment Center, 325 Broadway, Boulder, CO 80305-3337, USA, email: Tim.Fuller-Rowell@NOAA.gov.
[3]Senior Research Associate, The Cooperative Institute for Research in Environmental Sciences, University of Colorado, and the National Oceanic and Atmospheric Administration, Space Environment Center, 325 Broadway, Boulder, CO 80305-3337, USA, email: Mihail.Codrescu@NOAA.gov.

(LEO) (<100 km) satellites [1]. Furthermore, this region, the neutral atmosphere, also called the thermosphere (95 to 500 km altitude), is constantly changing, and as a result, the estimation of the drag perturbation has a large uncertainty. The neutral atmospheric density affects a satellite's trajectory through the generalized drag force equation described as

$$\boldsymbol{a}_{\text{drag}} = -\frac{1}{2} C_D A \rho \boldsymbol{v}_{\text{rel}} |\boldsymbol{v}_{\text{rel}}| / m \tag{1}$$

where $\boldsymbol{a}_{\text{drag}}$ is the perturbation acceleration vector due to drag, C_D is the dimensionless value for the drag coefficient and dependent on the shape of the satellite, A is the satellite's cross-sectional area, and m is the mass of the satellite. The vector, $\boldsymbol{v}_{\text{rel}}$, represents the satellite's velocity vector relative to the ambient neutral atmosphere, and ρ is the total mass density of the ambient neutral atmosphere. Equation (1) is a general representation a much more complicated process of translating the neutral atmospheric density into force on the spacecraft. Equation (1) can be further complicated by a number of sources including: unmodeled neutral winds, the atomic and molecular constituents and ionization of the atmosphere, heat dissipation, spacecraft shape, spacecraft tumbling, and others [2, 3, 4, 5, 6]. Although difficulties can arise in estimating any of the terms in the drag force equation (1), the density term, ρ, consistently has among the largest uncertainties. Any improvement in estimating of ρ would significantly improve the drag estimate and consequently improve one's estimate of the other orbital parameters, as tests show [7, 8].

To improve density estimates, several decades of research have focused on modeling the neutral atmospheric density. Empirical, or static models, of the upper atmosphere, like the Jacchia 70 [9], Jacchia 77 [10], the Mass Spectrometer and Incoherent Scatter Extension (MSIS-E-90) [11, 12, 13] and the Naval Research Laboratory MSIS (NRLMSIS-00) [14] models, are convenient ways to represent the neutral atmospheric density. These models provide the most-likely conditions of the neutral atmosphere, statistically calculated from a database of satellite, rocket, and ground observations over many years. Because the empirical model is a statistical representation of the climate over a long period of time (years, months), they may not appropriately represent unusual, short-term features (hours, minutes) in the upper atmosphere. These hourly or minute-to-minute features in the thermosphere become even more pronounced during geomagnetic storms. Past studies indicate errors in empirical models of 8 to 24% [15, 16]. Whereas other, more-recent studies indicate that errors for MSIS-90 may reach 30 to 50%, even during low solar activity [17], and NRLMSIS-00 can reach 30% at 200 km altitude and 70% at 600 km altitude [18], as some examples.

To account for this unmodeled variability in the empirical model, data assimilation techniques have been applied in recent years to correct these models using current observations [19, 20]. Data assimilation systems implement a solution method, which is oftentimes an inverse method like the least squares solution or a variation thereof [21]. In summary, the least squares method calculates a solution for the state based on the minimization of the sum of squares of the observation errors [22, 23, 24]. An example of one such system, which employs the least squares method, is the High Accuracy Satellite Drag Model (HASDM) [8, 19, 20, 25, 26], which provides an improved specification of the neutral density with errors typically below 7 to 8% [27].

In data assimilation systems, one primary source of neutral density observations comes from the space surveillance of LEO satellites. The surveillance of LEO satellites has been in use for several decades and is a well-documented and validated observation source for the neutral density, whose summary history can be found in Vallado [1]. HASDM, for example, assembles data from a large (60+ satellites) constellation of LEO satellites using satellite surveillance with plans to further increase the number of satellites [28]. Density is obtained by observing perturbations in these LEO satellites' orbital parameters. If the ballistic coefficient is estimated along with the other orbital parameters, changes in the estimated ballistic coefficient can indicate changes in the neutral density [19].

Observing a constellation of LEO satellites allows one to build a global, time-dependent map of the neutral density. However, the difficulty in using satellite surveillance arises from having to observe the satellite constellation over long periods, usually over many hours, to extract the changes in the ballistic coefficient estimate from the observation noise. In a validation study for the Dynamic Calibration Atmosphere (DCA) Phase I of HASDM [21], results indicate that only slight improvements could be obtained past a spherical harmonic resolution of degree 1 (2×2), with insignificant improvement beyond degree 2 (3×3) due to the long observation period requirement. To obtain this density resolution, according to Casali and Barker [21], the 0-degree correction to the exospheric temperature is solved every three hours. The higher-degree exospheric temperature coefficients are solved every 18 hours. Additionally, a 0-degree inflection temperature is solved for every 18 hours. A three-hour segmentation was sufficient in conjunction with an *a priori* uncertainty of 3% (RMSE), as is the best level of drag modeling thought to be statistically obtainable by DCA.

Research Objectives

To overcome the effects of a long observation period in space surveillance, this research examines the potential of other observation sources, which have a higher temporal resolution. Even though global coverage is reduced for two remote sensing satellites as compared to the 60+ satellites in space surveillance, the higher temporal resolution of remote sensing can help detect the minute-to-minute variability in the neutral atmospheric density.

This research seeks to answer the following two questions: (1) How well can the higher temporal resolution of two remote sensing satellites resolve the hourly and minute-to-minute variability? (2) Can the higher temporal resolution of only two remote sensing satellites provide a stable solution at a higher resolution as compared with the space surveillance? This research seeks to answer these questions according to the following procedure: a simulated thermosphere is created using a physical model, the Coupled Ionosphere-Thermosphere Model (CTIM) [29, 30, 31, 32], which is defined as the "truth" thermosphere. This truth thermosphere simulates 24 hours of quiet, followed by 12 hours of geomagnetic storm conditions, followed by another 12 hours of quiet to respectively examine the quiet, storm, and storm-recovery capability of the system. The storm conditions will reach an a_p index of 300 during the 12-hour storm. This truth thermosphere will be sampled using a satellite simulation algorithm [33] according to the orbital and instrument mechanics of two remote sensing observing systems, both of which are on two polar-orbiting satellites. Normalized random errors are added to the

observations of both satellites to simulate measurement noise; details are described is subsequent sections. These simulated observations are used to calculate the thermospheric density via a least squares solution. This solution is compared with the original truth thermospheric density. A root mean squared error (RMSE) and a pattern correlation coefficient are calculated to quantify the solution accuracy.

The solution resolution is limited by the amount of information contained in the observations. As one increases the resolution beyond this limit, numerical errors are introduced, and the system is said to be ill-conditioned [34, 35]. As a result, there is a maximum stable resolution that can be obtained for a given data set. When the solution becomes ill-conditioned, the functional description of the neural atmosphere may contain errors, particularly for the higher order terms. The maximum stable resolution is determined in this study by incrementally increasing the resolution until a limit on the maximum RMSE and minimum pattern correlation coefficients is found. The RMSE and pattern correlation coefficient results indicate that the higher temporal resolution of the two remote sensing satellites allows a stable solution, using the least squares method, up to degree 4 (5×5) every ten minutes. This resolution is an improvement compared with 60+ space surveillance satellites used in the DCA solution, which has a resolution of degree 2 (3×3) resolution every 18 hours and degree 0 (1×1) every three hours.

It should be brought to the reader's attention that several caveats exist concerning the ideal operation of the remote sensing system. Although the errors sources in space surveillance have been examined over several decades and are well-documented, remote sensing of the neutral density is a comparatively new field. Remote sensing error sources for the density/temperature are not yet well-understood and are only in the initial stages of study and documentation [36]. The observation errors in this study are assumed to be random, normalized, and uncorrelated in time. Any unmodeled biases in the actual remote sensing system will increase the errors indicated in this study. If the system errors in remote sensing can be described and modeled by current and on-going studies, the RMSE and pattern correlation coefficient values in this research can indicate the potential accuracy that remote sensing can provide for neutral density estimation. If other observation parameters, like neutral winds, are included in future data assimilation systems, then it is possible that the remote sensing accuracies can be further improved. Furthermore, the maximum stable resolution in the remote sensing solution should not be significantly affected since it is dependent on the remote sensing data rate and coverage, which are well-known. It is also expected that other observing systems with high temporal resolution, like *in situ* satellites, will provide similar results compared with remote sensing, and the results in this research can be used to support the potential of *in situ* measurements as well.

Variability in the Thermosphere

Regardless of the observing platform, time-dependent neutral atmospheric density estimation faces a number of challenges. External processes drive most of the variability in the upper atmospheric dynamics. During quiet times, the Sun slowly heats the upper atmosphere by solar radiation in the extreme ultraviolet (EUV) frequencies. EUV heating occurs on the sunlit side of Earth with the maximum heating occurring at the region nearest to the sub-solar point [37, 38].

Most of the hourly or minute-to-minute variability in the thermosphere arises from magnetospheric sources imposed at high latitudes. During geomagnetic storm

times, the nonlinear heating process becomes more complicated and even more spatially and temporally variable. Geomagnetic storms occur when material, ejected from the Sun by a coronal mass ejection or corotating stream, hits the Earth's magnetosphere. If the solar wind plasma has a southward magnetic field, it creates an efficient coupling with the magnetosphere. Initially, plasma convection increases and auroral particle precipitation expands to lower latitudes [38]. Besides the increased heating rate from particle precipitation and from Joule dissipation, the expanded convective electric field also redistributes the plasma [39, 40]. Substantial thermospheric changes under these conditions can occur within minutes.

As stated earlier, empirical models have greater difficulty representing this temporally and spatially varied structure due to their statistical representation of the global neutral atmosphere structure. To describe the variability, the empirical models must be corrected using observations with sufficiently high temporal and spatial resolutions.

Simulating Variability in the Neutral Atmosphere

Unlike empirical models, physical models are adept at reproducing short-term, small-scale variability, which is more representative of natural variations in the neutral density and is often missing in empirical models. To simulate this variability in the truth neutral atmosphere, the physical model, CTIM, is used. CTIM is a combination of two independently developed physical models. The first part of CTIM contains a global, nonlinear, time-dependent neutral atmospheric model developed at University College London [29, 30]. The second part contains a mid- and high-latitude ionospheric convection model that originated at Sheffield University [31]. The high latitude electric field [41] and auroral particle precipitation [42] are the two main high latitude inputs for the ionospheric-thermospheric coupled model, and these inputs determine the amount of Joule heating. The other main inputs are the solar ultraviolet and extreme ultraviolet radiation, which provide the bulk of the thermospheric heating and ionization.

CTIM was chosen to simulate the truth thermosphere since the code solves the nonlinear equations of momentum, energy, and continuity to provide a time-dependent structure of the wind vector, temperature, and density in the neutral atmosphere. As a result, the simulation from a physical model provides a more varied, smaller-scale structure in comparison to the statistically averaged structure provided by empirical models [43]. It is not expected that the physical model will reproduce the exact conditions that occurred on the days simulated in this research. In fact, it is expected that CTIM will have about the same error level in representing the actual conditions for these days as the empirical model. However, CTIM can simulate greater variability than the empirical model, and the amount of variability is properly simulated in the truth thermosphere. This difference in structure between the empirical and physical model types resembles the expected differences in variability between the empirical model and actual variations in the neutral atmosphere. Observing this simulated variability and trying to correct the smoother empirical model test the data assimilation system's ability to discern the variability for the given the observation system.

Observing the Density Using Remote Sensing

As already stated, remote sensing instruments provide high temporal and spatial resolution as compared with space surveillance. Like space surveillance, remote

sensing observations may also be used in the batch least squares solution to estimate the neutral density. One example of remote sensing measures the vertical profile of ultraviolet airglow from different species. The vertical profiles can be used to estimate species density which can also be used to infer temperature from the scale height of the altitude distribution. This research focuses on two particular spectrographic instruments: the Special Sensor Ultraviolet Limb Imager (SSULI) [44], and the Special Sensor Ultraviolet Spectrographic Imager (SSUSI) [45, 46, 47]. These particular instruments are chosen for this study since these or similar instruments are under consideration for deployment in the National Polar-Orbiting Operational Environmental Satellite System (NPOESS). The SSULI and SSUSI instruments were developed for the Defense Meteorological Satellite Program (DMSP) Block 5D4 satellites. The DMSP Block 5D4 satellites maintain a near polar, Sun synchronous orbit at an altitude of approximately 830 km.

SSUSI, developed by the Applied Physics Laboratory, APL, at Johns Hopkins University and by Computational Physics, Inc., [45, 46, 47], is designed to measure numerous parameters of the upper atmosphere including the neutral species densities and auroral effects by detecting far ultraviolet natural airglow radiation from atoms, molecules, and ions in the upper atmosphere. The imager uses a scanning mirror to infer number density profiles of the major species O, O_2, and N_2 on the limb and height integrated properties at the Earth's disc. The Scanning Imaging Spectrograph [45] device of the SSUSI instrument, builds a spectrographic image by scanning across the satellite's ground track, from limb-to-limb as shown in Fig. 1.

During this scan, the scan mirror sweeps the field-of-view by rotating between ± 72.8 degrees. The instrument receives a cross-track scan every 22 seconds. A scan cycle consists of a limb viewing and an Earth viewing part. The limb viewing occurs above the horizon from the maximum scan angle of ± 63.2 degrees from nadir to the horizon ± 63.2 degrees from nadir. The Earth viewing occurs between

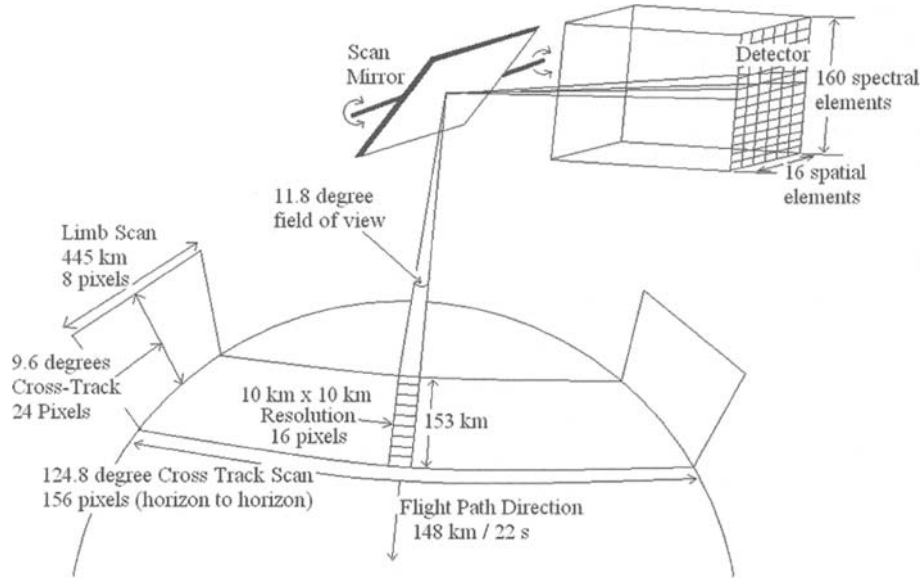

FIG. 1. The Scanning Imaging Spectrograph Conducting a Horizon-to-Horizon Limb Scan.

the limb scans or between ±63.2 degrees from nadir creating a field of view about 445 km. In a near-circular orbit at an altitude of about 830 km, the satellite moves 148 km for each 22-second scan. With a satellite at 830 km altitude, the maximum height above the horizon is about 520 km if the maximum scan angle is ±72.8 degrees. It is assumed in this research that species' density profiles are obtained only on the limb portions of the scan.

SSULI is an optical remote sensor developed by the Naval Research Lab [44]. Unlike the SSUSI instrument, the SSULI instrument only looks towards the Earth's limb to infer the species' density profiles. SSULI obtains the vertical profiles by viewing between tangent altitudes of approximately 50 to 750 km. As the SSULI instrument scans along this altitude range, the extreme and far ultraviolet airglow from atoms, molecules, and ions are recorded as a function of altitude.

The limb scanner faces in the opposite direction of the satellite flight path vector, as shown in Fig. 2. The field-of-view is 0.1 degrees in the vertical and 2.4 degrees in the horizontal direction. The entire scan covers 30 degrees in the vertical by 2.4 degrees in the horizontal direction. The scan ranges from 10 to 40 degrees below the satellite's flight direction of and lasts five seconds with a scan every ten seconds.

One should keep in mind that these instrument definitions are a generalization of the more complicated process of converting the raw measurement of the ultraviolet intensity to realistic values for the total neutral density. However, the focus of this research is to emphasize the importance of instrument resolution as opposed to raw data conversion techniques. The orbital and instrument scanning mechanics, on the other hand, have not been generalized and simulate the observing platforms according to their design.

DMSP satellites typically follow a Sun-synchronous orbit. The simulation in this research uses two Sun-synchronous satellites, each carrying one SSULI and one SSUSI instrument, which pass the ascending nodes at 0930 and 1330 local time (LT). In the present study, it is assumed that the instrument provides an exospheric

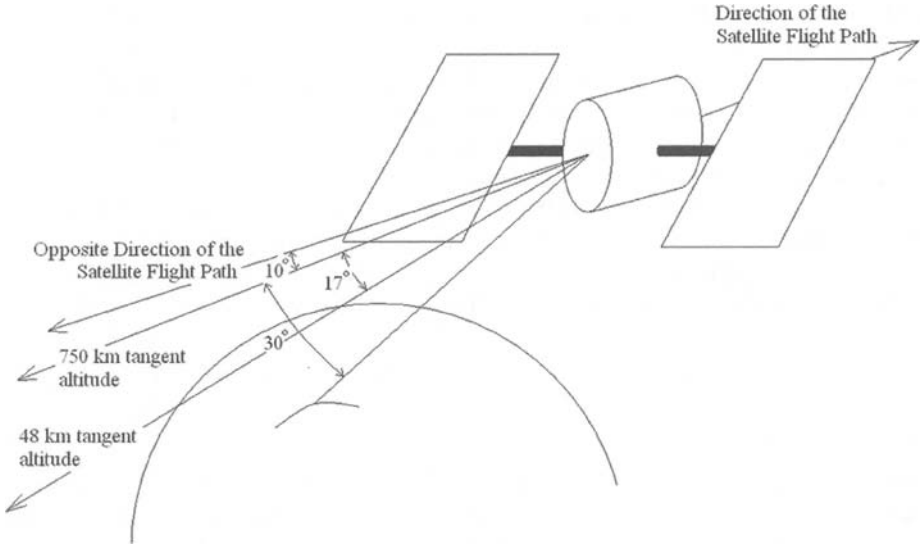

FIG. 2. The Special Sensor Ultraviolet Limb Imager Conducting a Limb Scan.

temperature, which can be translated into density as a function of altitude through an empirical model. A daytime fixed error of 15% is applied as measurement noise via a random number generator. This representation of the error is approximately two to three times higher than what is estimated by the instrument designers to insure that the error standard deviation covers the possible range as a "worst-case" scenario to test the data assimilation system. Otherwise, this error does not include anomalous effects and is a summation of the average error from all of the instrument's components, effects external to the instrument, and various stages of the data processing. In this research, the remote sensing observation rate is one observation every 0.1 seconds for both instruments, and each satellite carries one SSULI and one SSUSI instrument. To resemble the capabilities of the current remote sensing systems, measurements are simulated on the dayside only.

It is expected that remote sensing from only two remote sensing satellites will have limited global coverage, i.e. all local times cannot be observed at a given instant. As a result, rapidly changing conditions during geomagnetic storms may not be observed, particularly as only dayside observations are available. The lack of global coverage from only two remote sensing satellites is the reason that the spherical harmonic resolution is limited to degree 4 (5×5).

Solution Method

The atmospheric density corrections using remote sensing data can be generalized as a minimum variance estimation problem [24], which can be formulated as follows:

Given:

$$\mathbf{y}_k = H_k \hat{\mathbf{X}}_k + \boldsymbol{\varepsilon}_k$$

where $\boldsymbol{\varepsilon}_k$ is the error on the observation, which is assumed to have a zero mean and specified covariance, R_k.

Find: the linear, unbiased estimate, $\hat{\mathbf{X}}_k$, at a specified time, k, that has the minimum variance. The state, $\hat{\mathbf{X}}_k$, contains the coefficients $a_{i,j}$, $c_{i,j}$, and $s_{i,j}$ where i is the degree and j is the order of the spherical harmonic as described in equation (2); $\mathbf{y}_k$ denotes the measurement of the exospheric temperature, $T(\psi, \lambda)$, at a given latitude and longitude from the remote sensor; H_k denotes the measurement-state relationship; and R_k denotes the covariance matrix of observation errors.

The elements in $\hat{\mathbf{X}}_k$ represent the coefficients of a series of spherical harmonics representing the neutral atmospheric temperature or total density. The value for the neutral temperature, T, for example, at a specific latitude, ψ, and longitude, λ, expanded in spherical harmonics [48], may be written as

$$T(\psi, \lambda) = a_0 + \sum_{i=1}^{\infty} a_i [P_i(\sin \psi)] + \sum_{i=1}^{m} \sum_{j=1}^{i} [P_{i,j}(\sin \psi)]\{c_{i,j} \cos(j\lambda) + s_{i,j} \sin(j\lambda)\} \tag{2}$$

where a_0, a_i, $c_{i,j}$, and $s_{i,j}$ are the spherical harmonic coefficients, contained in the state vector, $\hat{\mathbf{X}}_k$, to be estimated. In this paper, "degree m" means that all degree and order coefficients up to m, as described in equation (2). P_i and $P_{i,j}$ are Legendre polynomials such that

$$P_i(\sin\psi) = \frac{1}{2^i i!}\frac{d^i}{d(\sin\psi)^i}[(\sin\psi)^i - 1]^i$$

and

$$P_{i,j}(\sin\psi) = [1 - (\sin\psi)^2]^{j/2}\frac{d^j P_i}{d(\sin\psi)^j}$$

The spherical harmonic equations and the estimates of the associated coefficients allow for a functional representation of the exospheric temperature at any point on the globe. Although the structure of the neutral atmosphere is varied, it is also naturally continuous, and therefore, implementing the continuous function using the spherical harmonics is an appropriate representation. Once the global temperature is estimated, this estimate can be converted to density through an empirical model. In the context of this paper, exospheric temperature and density are assumed to be interchangeable.

To solve the minimum variance problem, a least squares solution is applied [22, 23, 24]. The least squares technique is used in this research, as opposed to Kalman filters or variational methods, to follow currently operating data assimilation systems for the neutral density. As stated earlier, the least squares method calculates a solution for the state based on the minimization of the sum of squares of the observation errors. The least squares solution is generalized for the problem presented here as

$$\hat{\mathbf{X}}_k = (H_k^{\mathrm{T}} R_k^{-1} H_k + \bar{P}_k^{-1})^{-1}(H_k^{\mathrm{T}} R_k^{-1}[\mathbf{y}_k - \mathbf{y}_k^*] + \bar{P}_k^{-1}[\bar{\mathbf{X}}_k - \mathbf{X}_k^*]) + \mathbf{X}_k^* \quad (3)$$

where $\mathbf{y}_k$ represents the observation data, and $\mathbf{y}_k^*$ contains the expected observations based on the defined nominal state. The state vectors include the following: $\bar{\mathbf{X}}_k$, the *a priori,* or best estimate of the state before the least squares calculation is performed; $\mathbf{X}_k^*$, the nominal state; and $\hat{\mathbf{X}}_k$, the new least squares estimate for the state for a given batch of observations at a given epoch, k. The *a priori* state, $\bar{\mathbf{X}}_k$, can contain either the initial conditions, which are usually obtained from the defined empirical model, or the current state estimate based on a previous batch of data. Associated with the *a priori* state is the *a priori* error variance-covariance matrix, $\bar{P}_k$, whose diagonals are an indicator of the amount of error variance in the state. The off-diagonal terms in $\bar{P}_k$ indicate the amount of covariance between any two elements in $\bar{\mathbf{X}}_k$. $\bar{P}_k$ is initialized based on the expected amount of error in the nominal state. The error variance-covariance matrix can be updated with each new batch of data as

$$P_k = (H_k^{\mathrm{T}} R_k^{-1} H_k + \bar{P}_k^{-1})^{-1} \quad (4)$$

where P_k is the new state error variance-covariance matrix based on the new state from least squares result. After the new state, $\hat{\mathbf{X}}_k$, and its associated error variance-covariance matrix, P_k, are calculated, this state and associated error matrix replace the *a priori* state, $\bar{\mathbf{X}}_k$, in equation (3) and the *a priori* state error variance-covariance matrix, $\bar{P}_k$, in equation (4). The least squares solution may be recalculated to provide an improved solution. The solution can be further improved by iterating this process. The least squares solution typically converges after two to four iterations with no substantial improvement thereafter.

The least squares solution may ingest a batch of data over a given span of time to estimate the state at a single specified epoch, k. The matrix and vector terms, $H_k^{\mathrm{T}} R_k^{-1} H_k$ and $H_k^{\mathrm{T}} R_k^{-1} \mathbf{y}_k$, in equation (3) may be accumulated as

$$H_k^{\mathrm{T}} R_k^{-1} H_k = \sum_{l=1}^{m} \tilde{H}_l^{\mathrm{T}} R_l^{-1} \tilde{H}_l$$

and

$$H_k^{\mathrm{T}} R_k^{-1} [\mathbf{y}_k^{\mathrm{obs}} - \mathbf{y}_k^*] = \sum_{l=1}^{m} \tilde{H}_l^{\mathrm{T}} R_l^{-1} [\mathbf{y}_l^{\mathrm{obs}} - \mathbf{y}_l^*]$$

where $\tilde{H}_l$ is the observation-specific mapping matrix for the lth observation, R_l is the lth observation covariance matrix, $\mathbf{y}_l^{\mathrm{obs}}$ is an individual observation, and $\mathbf{y}_l^*$ is the empirically expected observation at time l.

Associated with the observation vector, R_l is the observation error covariance matrix that contains an estimate of the uncertainty in $\mathbf{y}_l^{\mathrm{obs}}$. R_l is estimated before the least squares method is applied. The diagonals of R_l represent the error variance in the observations defined by the instrument and observation system accuracy. The off-diagonals in R_l are assumed to be zero, meaning there are no correlations in the observation errors.

If the amount of information required to describe a given solution resolution exceeds the amount of information available in the observations, a linear dependence will occur in the system of equations to be solved, and the system is said to be ill-conditioned [34, 35]. In an ill-conditioned system, the matrix to be inverted in equation (3) is close to singular, i.e. one or more eigenvalues are close to zero, and the inversion cannot be computed without introducing numerical errors. The inclusion of the state error variance-covariance matrix, $\bar{P}_k$, helps stabilize the inversion, but in ill-conditioned systems, the solution is very sensitive to the choice for $\bar{P}_k$ [49]. Providing an accurate estimate for $\bar{P}_k$ may be difficult, particularly if $\bar{P}_k$ is constantly changing with the dynamic neutral atmosphere. As a result, there is a limitation on the achievable resolution based on the amount of information contained in the observations. The results in this research indicate that two remote sensing satellites provide sufficient information to calculate a solution up to degree 4 (5×5) every ten minutes. Increasing the resolution further introduces numerical errors, particularly in the higher order terms of equation (2), offsetting the benefits of the increased resolution.

Evaluating the System Using Two Remote Sensing Satellites

For results analysis, the solutions are scored on how well they reproduce the defined truth thermosphere through a standard root mean square error, RMSE, and pattern correlation calculation, γ. The RMSE between the truth file and the least squares estimated state is calculated as

$$\mathbf{RMSE} = \sqrt{\sum_{n=1}^{N} (\hat{\rho}_n - \rho_n^{\mathrm{CTIM}})^2 / N} \tag{5}$$

where $\hat{\rho}_n$ is the estimated density at a particular grid point, n, and ρ_n^{CTIM} is the corresponding nth grid point of the CTIM-defined truth density. N is the total number of grid points.

The RMSE calculation is a useful tool for calculating the overall error in the estimate, but the RMSE provides no insight as to how well the solution pattern matches the true structure. The accuracy of the solution's structure can be quantified through the calculation of a pattern correlation coefficient [50]. This pattern correlation coefficient, γ, may be calculated as

$$\gamma = \mathrm{cov}(\hat{\boldsymbol{\rho}}, \boldsymbol{\rho}^{\mathrm{CTIM}})/\sqrt{\mathrm{var}(\hat{\boldsymbol{\rho}}) \cdot \mathrm{var}(\boldsymbol{\rho}^{\mathrm{CTIM}})} \tag{6}$$

where $\mathrm{cov}(\hat{\boldsymbol{\rho}}, \boldsymbol{\rho}^{\mathrm{CTIM}})$ is the covariance between the estimated, $\hat{\boldsymbol{\rho}}$, and true, $\boldsymbol{\rho}^{\mathrm{CTIM}}$, patterns and is calculated as

$$\mathrm{cov}(\hat{\boldsymbol{\rho}}, \boldsymbol{\rho}^{\mathrm{CTIM}}) = \sum_{n=1}^{N} [(\hat{\rho}_n - \hat{\mu}^{\mathrm{CTIM}})]/N$$

and the variance in the estimate as

$$\mathrm{var}(\hat{\boldsymbol{\rho}}) = \sum_{n=1}^{N} (\hat{\rho}_n - \hat{\mu})^2/N$$

and the variance in the truth state as

$$\mathrm{var}(\boldsymbol{\rho}^{\mathrm{CTIM}}) = \sum_{n=1}^{N} (\rho_n^{\mathrm{CTIM}} - \hat{\mu}^{\mathrm{CTIM}})^2/N$$

If the state estimate from the data assimilation system provides an accurate representation of the true structural pattern, then a correlation coefficient calculation will have a value close to but not exceeding one. Having a correlation coefficient of exactly one represents an exact correlation. If the estimated structure does not match the truth, then a correlation coefficient near zero will result. Ideally, one would wish to obtain a pattern correlation coefficient that is as close to one as possible.

Illustrative Example

A two-day period, at spring equinox, is simulated to provide the test case. An equinox scenario provides a thermosphere where roughly equal heating of the Southern and Northern Hemispheres exists. The test case simulates a 24-hour period of low geomagnetic activity with an energy input of about 10 GW, which is approximately equal to an a_p index of about 7. After the 24-hour quiet period, a 12-hour geomagnetic storm with a power input of about 260 GW follows, equivalent to an a_p index of approximately 300. After this 12-hour storm period, another 12-hour quiet time period, with an a_p of 7, follows. The total simulation period covers 48 hours. The results, during the quiet period from 0 to 24 hours, demonstrate the quiet-time accuracy of the least squares solution during undisturbed conditions. At 24 hours, the geomagnetic storm commences. During the 12-hour storm period, from hour 24 to 36, the data assimilation system must then react to rapidly changing conditions, increased winds, density variations, etc. The final 12 hours of quiet, from hour 36 to 48, demonstrate the recovery characteristics of the least squares solution, during which the composition is still changing as it recovers from the storm to quiet conditions.

The remote sensing observing system considers a combination of two Sun-synchronous satellites, with 09:30 and 13:30 LT crossings. Both SSULI and SSUSI instruments are simulated to take one measurement every 0.07 seconds, where SSUSI is viewing only on the limb. The SSUSI instrument is simulated to take observations only on the limb. The measurement error of the temperature is assumed to have a standard deviation roughly 15% for both SSULI and SSUSI instruments in daylight, and it is assumed that no measurements are available on the night side. The observation platform is summarized in Table 1.

TABLE 1. Summary of the Remote Sensing System

Solution Type	Number of Satellites	Observation Source	Observation Parameter	Inferred Observation	Observation Rate	Standard Deviation of Noise Added to each Observation
remote sensing (empirical model corrected using remote sensing via a least squares solution)	2 Sun-synchronous satellites—09:30 and 13:30 LT crossings	timely observations from 1 SSULI and 1 SSUSI instrument on each satellite	UV airglow intensity (dayside only)	temperature from which density can be obtained	1 measurement/ 0.07 seconds	15%

RMS Errors Results

To quantify the average accuracy of the data assimilation system, the RMSE over the entire globe is computed, according to equation (5). The RMSE values for various resolutions for the spherical harmonic representation are shown in Fig. 3. The figure demonstrates that accuracy improves with increasing resolution from degree 0 (1×1) to 4 (5×5). No significant improvements are observed with increasing resolution beyond degree 4. For degree 5 and higher, numerical errors from the ill-conditioning offset any benefits from the increased resolution.

The degree 0 result is simply a global correction to the empirical model. In other words, the entire density structure estimated by the empirical model is adjusted uniformly. The large variations in the RMSE for degree 0 for all phases indicate an inability to capture the overall global structure. The storm and recovery between 24 and 42 hours increase in RMSE indicates the inability to capture the storm and recovery conditions at this low resolution.

The degree 2 case contains corrections to the structure of the empirical model based on a 3×3 grid. Degree 2 matches the maximum stable resolution obtained by Casali and Barker for the 60-satellite space surveillance study [21]. The degree 2 case in Fig. 3 shows an overall improvement in the average RMSE between the quiet, storm, and recovery phases as compared to degree 0, indicating an improved ability to distinguish the overall global structure. The higher degree 2 resolution shows improvement in capturing the storm and recovery effects as the RMSE during this period between 24 and 42 hours is now reduced.

The RMSE for the degree 4 case (5×5) in Fig. 3 shows further improvement in the quiet, storm, and recovery solution accuracy. Although the RMSE increases during the storm for degree 4, the comparatively lower RMSE during all phases indicates improved overall accuracy, including storm and recovery. The influence of the storm becomes apparent at the storm's end (hour 36) in comparison with the quiet-time RMSE. The RMSE during the storm, between hours 24 and 36, increases slightly as the thermosphere becomes increasingly disturbed as the storm progresses. During the storm, the increase in RMSE illustrates the limitation of two-satellite remote sensing coverage when trying to capture the rapidly changing storm-time structure. In other words, storm-induced changes are occurring in the

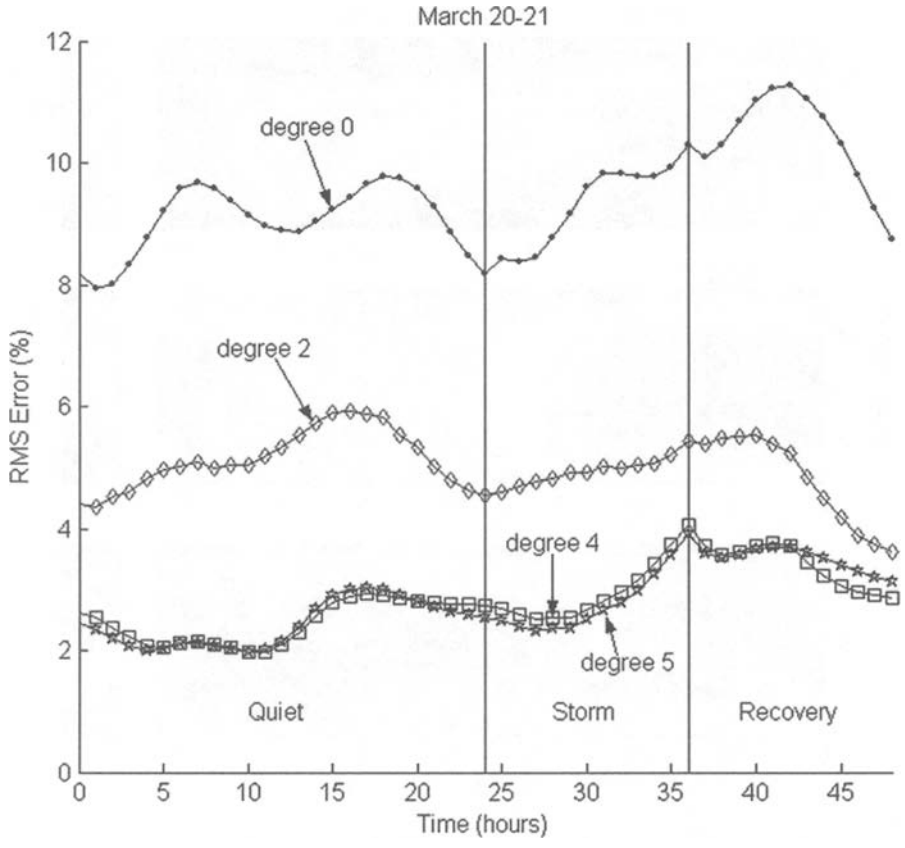

FIG. 3. Time-Dependent RMS Errors in Temperature for the Remote Sensing Simulation Using a Two Sun-Synchronous Satellites at 09:30 and 13:30 LT Crossing for Varying Spherical Harmonic Resolutions.

unobserved regions. Overall, however, the two remote sensing satellites still provide enough information to provide a stable degree 4 resolution and provide an improvement over the degree 2 case for all periods, including the storm's peak.

Figure 4 is provided to help visualize the truth thermosphere (top panel), the resolution of the degree 4 result (middle), and absolute difference (bottom) between the truth and the degree 4 result. The top panel shows the exospheric temperature in Kelvin for the truth thermosphere at the storm's end (hour 36). The top panel illustrates the auroral heating at the end of the 12-hour storm, indicated by the large, red (high temperature) regions at high latitudes. The middle panel shows the degree 4 least squares solution for the two-satellite remote sensing case, also at storm's end. The solution in the middle panel appears "smooth" because of the ill-conditioning limitation in the resolution. The least squares solution in the middle panel does, however, resemble the general structure of the top panel with solar heating on the dayside (between 130 and 310 degrees longitude) and heating due to the storm at higher latitudes, but much of the finer structure is missing. The bottom panel shows the absolute difference between the truth top panel and the remote sensing solution middle panel. Red areas in the bottom panel indicate regions of high error, and blue areas indicated regions of low error. Red areas particularly at the higher latitudes are shown in the bottom panel of Fig. 4 indicating increased

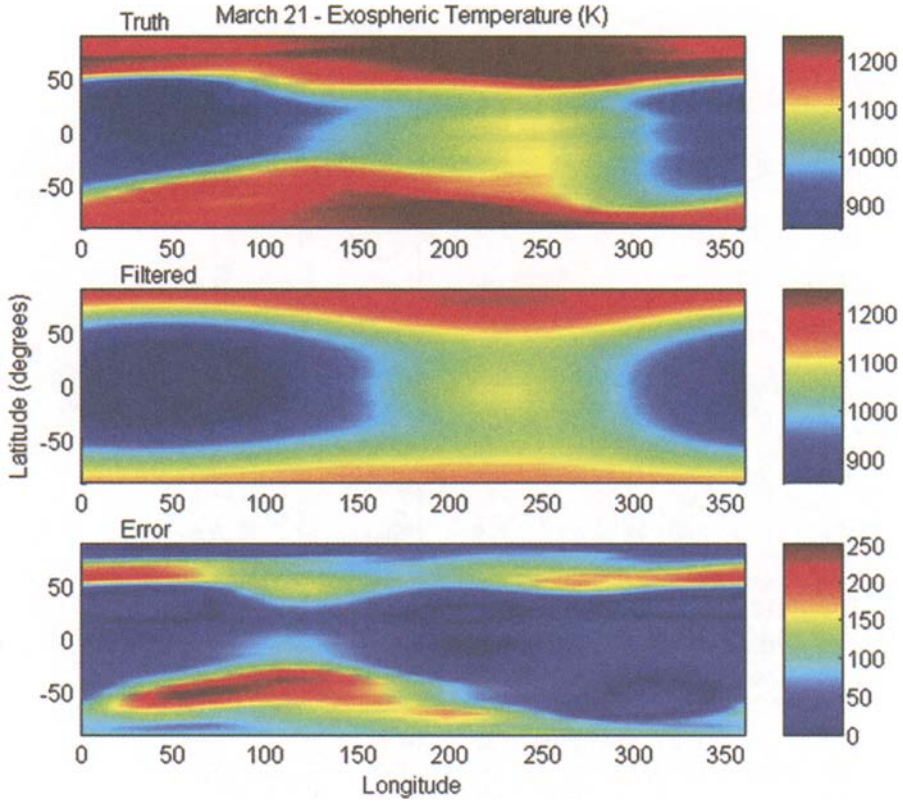

FIG. 4. Exospheric Temperature by Remote Sensing Using Two Sun-Synchronous Satellites at 09:30 and 13:30 LT Crossing for Degree 4 (5 × 5) Spherical Harmonic Resolution at Equinox at Hour 36.

errors in these regions due to limited coverage and the inability to observe all of the storm-induced changes. The bottom panel of Fig. 4 shows the largest error on the night side since the remote sensing satellites are assumed to take no observations on the night side. Some dayside errors still exist but are smaller in comparison.

Correlation Patterns Results

Although the RMS error calculations provide a way of estimating average global accuracy, the correlation pattern coefficient, γ, equation (6), provides insight into how well the data assimilation solution structurally represents the truth thermosphere. Pattern correlation coefficient results are shown in Fig. 5 for varying spherical harmonic resolution.

Like the RMSE calculations in Fig. 3, the pattern correlation coefficient calculations in Fig. 5 also show improvements in accuracy for increasing resolution. A maximum resolution, again, is reached at degree 4 (5 × 5), with no significant improvement for higher degrees as a result of ill-conditioning.

The degree 0 (1 × 1) and 2 (3 × 3) results show significantly varying pattern correlation coefficients during the quiet, storm, and recovery phases. The degree 0 and 2 resolutions appear almost random in Fig. 5. These variations can be attributed to the inability of this resolution to represent the global structural patterns. Degree 2 demonstrates some ability to distinguish differences between the quiet,

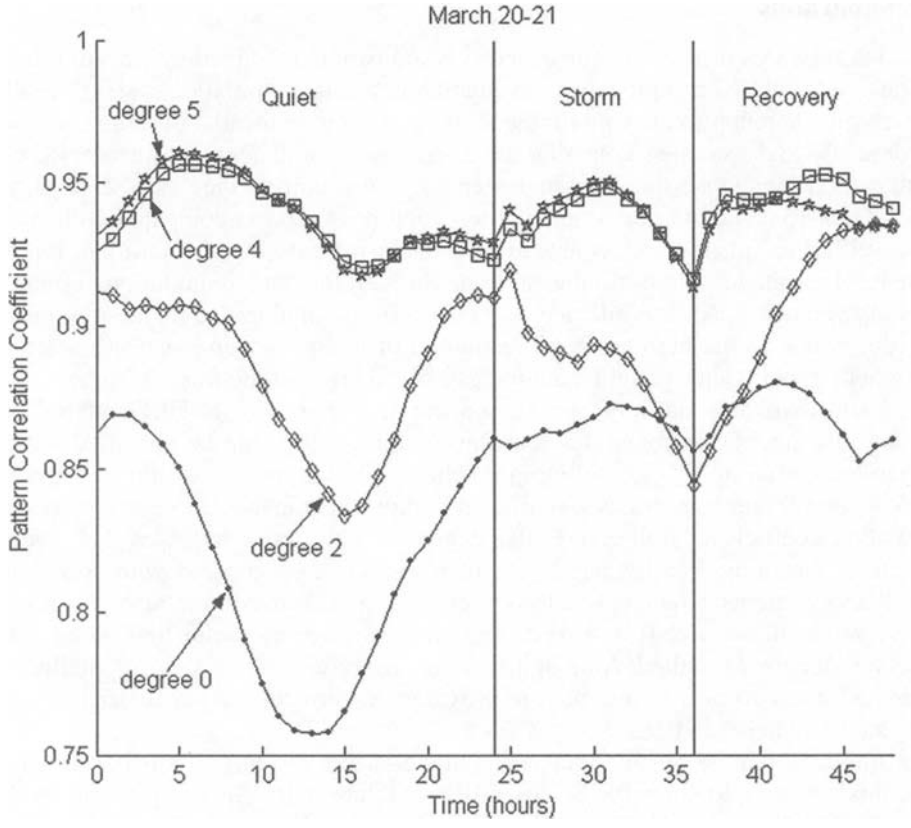

FIG. 5. Time-Dependent Pattern Correlation Coefficient for the Remote Sensing Simulation for Varying Spherical Harmonic Resolutions.

storm, and recovery phases. For degree 2, the pattern correlation coefficient does decrease during the storm period and increases again during recovery, although the correlation coefficient fluctuates significantly with time. The seemingly random variations for degree 0, on the other hand, demonstrate an almost complete inability to distinguish between the quiet and storm density/temperature structural patterns.

Increasing the resolution to degree 4 appears to improve the structural representation in the solution as the variation in the correlation with time is reduced. The decrease in the correlation at the storm's end is distinct, although the correlation appears to vary during the course of the storm as well as during quiet times. The variations in the degree 4 resolution can be attributed to the limited global coverage provided by two remote sensing satellites. As stated earlier, two satellites cannot observe the entire globe at any given time, and storm-induced changes in unobserved regions will lead to poorer pattern correlation coefficients in specifying the global structure.

Although limitations exist in the remote sensing system, two remote sensing satellites do indicate a high overall pattern correlation coefficient with values consistently above 0.92. The pattern correlation coefficient is typically less affected by instrument errors, as compared to RMS, since it more indicative of the amount of instrument and satellite coverage, which can be accurately determined and should closely match actual instrument-satellite systems.

Conclusions

This research provides an introductory examination into the usefulness of remote sensing for global neutral density estimation in a data assimilation system. Results presented herein provide a preliminary measure for the potential of remote sensing for its use in discerning the small-scale, short-term neutral density structure. Results show that remote sensing may be better adept at capturing the small-scale, short-term density structure due to its high temporal resolution as compared with space surveillance. This research comes to this conclusion based on the ability of remote sensing to obtain a higher stable solution through the data assimilation system as compared with space surveillance. The effects of ill-conditioning in the solution are reduced due to the high temporal resolution of remote sensing, and ultimately, a higher temporal and spatial resolution can be achieved in the final estimate.

Using two dayside-only remote sensing satellites with SSULI and SSUSI-type instruments demonstrates that the neutral density can be specified with a stable solution up to and including a spherical harmonic resolution of degree 4 (5×5) every ten minutes. No significant improvement in the RMSE or pattern correlation coefficient is observed after degree 4. This result indicates that remote sensing can provide a higher degree of resolution as compared with space surveillance systems, which have a lower degree 2 (3×3) maximum resolution every 18 hours with a degree-0 (1×1) correction every three hours due to the longer observation period required. Although coverage from two remote sensing satellites is limited, the coverage is sufficient to provide a pattern correlation coefficient consistently higher than 0.92.

Although remote sensing indicates a higher stable resolution, it is not possible, in this research, to know the quality of this resolution. RMSE and pattern correlation coefficients are calculated in this research to provide some guidance in the overall accuracy of the density estimates, but these results pertain to a simulated thermosphere with simulated instruments. This research assumes ideal observation conditions, i.e. no data loss, normalized errors, no unmodeled biases, no time-correlations, etc. To make a proper comparison with space surveillance from an accuracy point-of-view, while not considering resolution alone, a more rigorous study is required, most likely with actual data. However, at a minimum, these results provide some baseline for analyzing remote sensing systems and future observing sources. These results therefore indicate the potential usefulness for remote sensing as additional observation source in the continual expansion and development of current data assimilation systems. The results presented here also support the use of other observation sources, like *in situ* observations, that provide data with a high temporal and spatial resolution.

Acknowledgments

This work was supported by the United States Department of Defense, the United States Air Force, and the Air Force Office of Scientific Research, award number F49620-02-1-0178.

References

[1] VALLADO, D. A. *Fundamentals of Astrodynamics and Applications,* McGraw-Hill Companies, Inc., New York, 1997, pp. 485–525, 651–658.

[2] ALFONSO, G., BARLIER, F., BERGER, C., MIGNARD, F., and WALCH, J. J. "Reassessment of the Charge and Neutral Drag of LAGEOS and its Geophysical Implications," *Journal of Geophysical Research,* Volume 90, 1985, pg. 9381.

[3] RUBICAM, D. P. "Drag on the LAGEOS Satellite," *Journal of Geophysical Research,* Volume 95, B4, 1990, pg. 4881.

[4] FRITSCHE, B. and KLINKRAD, H. "Accurate Prediction of Non-Gravitational Forces for Precise Orbit Determination—Part I: Principles of the Computation of Coefficients of Force and Torque," presented as paper AIAA-2004-5461 at the AIAA/AAS Astrodynamics Specialist Conference and Exhibit, Providence, Rhode Island, August 16–19, 2004.

[5] FRITSCHE, B. and KLINKRAD, H. "Accurate Prediction of Non-Gravitational Forces for Precise Orbit Determination—Part II: Determination of Perturbing Forces and Torques in an Orbital Environment," presented as paper AIAA-2004-5462 at the AIAA/AAS Astrodynamics Specialist Conference and Exhibit, Providence, Rhode Island, August 16–19, 2004.

[6] DOORNBOS, E., SCHARROO, R., KLINKRAD, H., ZANDBERGEN, R., and FRITSCHE, B. "Improved Modelling of Surface Forces in the Orbit Determination of ERS and ENVISAT," *Canadian Journal of Remote Sensing,* Volume 28, Number 4, 2002, pp. 535–543.

[7] MARCOS, F. A., BASS, J. N., LARSON, D. R., LIU, J. J., and ROBINSON, E. C. "Satellite Drag Model Calibration and Feedback for Precision Low Earth Orbit Determination," *Proceedings of the 1997 Space Control Conference,* MIT Lincoln Laboratory, L. B. Spence, ed., Lexington, Massachusetts, 1997.

[8] MARCOS, F. A., KENDRA, M. J., GRIFFIN, J. M., BASS, J. N., LARSON, D. R., and LIU, J. J. "Precision Low Earth Orbit Determination Using Atmospheric Density Calibration," *The Journal of the Astronautical Sciences,* Volume 46, Number 4, October–December 1998, pp. 395–409.

[9] JACCHIA, L. G. "Revised Static Models of the Thermosphere and Exosphere with Empirical Temperature Profiles," *Smithsonian Astrophysical Observatory Special Report,* Number 313, 1970.

[10] JACCHIA, L. G. "Thermospheric Temperature, Density, and Composition: New Models," *Smithsonian Astrophysical Observatory Special Report,* Number 375, 1977.

[11] HEDIN, A. E. "A Revised Thermospheric Model Based on Mass Spectrometer and Incoherent Scatter Data: MSIS-83," *Journal of Geophysical Research,* Volume 88, 1983, pp. 10, 170-10, 188.

[12] HEDIN, A. E. "MSIS-86 Thermospheric Model," *Journal of Geophysical Research,* Volume 92, Number A5, 1987, May 1, 1987, pp. 4649–4662.

[13] HEDIN, A. E. "Extension of the MSIS Thermosphere Model into the Middle and Lower Atmosphere," *Journal Geophysical Research,* Volume 96, 1991, pp. 1159–1172.

[14] PICONE, J. M., HEDIN, A. E., DROB, D. P., and AIKIN, A. C. "NRLMSISE-00 Empirical Model of the Atmosphere: Statistical Comparisons and Scientific Issues," *Journal of Geophysical Research,* 107(A12), doi:10.1029/2002JA009430, 2002, pp. 1468–.

[15] LIU, J. F. "Advances in Orbit Theory for an Artificial Satellite with Drag," *The Journal of the Astronautical Sciences,* Volume 31, Number 2, April-June 1983, pp. 165–188.

[16] MARCOS, F. A. "Accuracy of Atmospheric Drag Models at Low Satellite Altitudes," *Advanced Space Research,* Volume 10, Number 3, 1990, pp. 417–422.

[17] PARDINI, C. and ANSELMO, L. "Calibration of Semi-Empirical Atmosphere Models through the Orbital Decay of Spherical Satellites," presented as paper 99-384 at the AAS/AIAA Astrodynamics Specialist Conference, Girdwood, Alaska, August 15–19, 1999.

[18] YURASOV, V. S., NAZARENKO, A. I., CEFOLA, P. J., and ALFRIEND, K. T. "Results and Issues of Atmospheric Density Correction," *The Journal of the Astronautical Sciences,* Volume 52, Number 3, July–September, 2004, pp. 281–300.

[19] BOWMAN, B. R. "True Satellite Ballistic Coefficient Determination for HASDM," presented as paper AIAA-2002-4887 at the AIAA/AAS Astrodynamics Specialist Conference and Exhibit, Monterey, California, August 5–8, 2002.

[20] STORZ, M., BOWMAN, B., and BRANSON, J. "High Accuracy Satellite Drag Model (HASDM)," presented as paper AIAA-2002-4886 at the AIAA/AAS Astrodynamics Specialist Conference and Exhibit, Monterey, California, August 5–8, 2002.

[21] CASALI, S. J. and BARKER, W. N. "Dynamic Calibration Atmosphere (DCA) for the High Accuracy Satellite Drag Model (HASDM)," presented as paper AIAA-2002-4888 at the AIAA/AAS Astrodynamics Specialist Conference and Exhibit, Monterey, California, August 5–8, 2002.

[22] LAWSON, C. L. and HANSON, R. J. *Solving Least Squares Problems,* Prentice Hall, 1963.

[23] LIEBELT, P. B. *An Introduction to Optimal Estimation,* Addison-Wesley, New York, 1967.

[24] TAPLEY, B. D., SCHUTZ, B. E., and BORN, G. H. "Fundamentals of Orbit Determination: The Sequential Estimation Algorithm," Statistical Orbit Determination, Chapter 4, Academic Press, 2004.

[25] BOWMAN, B. R. and STORZ, M. F. "High Accuracy Satellite Drag Model (HASDM) Review," presented as paper AAS 03-625 at the AIAA/AAS Astrodynamics Specialist Conference and Exhibit, Big Sky, Montana, August 3–7, 2003.

[26] STORZ, M. F. "HASDM Validation Tool Using Energy Dissipation Rates," presented as paper AIAA-2002-4889 at the AIAA/AAS Astrodynamics Specialist Conference and Exhibit, Monterey, California, August 5–8, 2002.

[27] WISE, J. O., MARCOS, F. A., BOWMAN, B., KENDRA, M. J., and BASS, J. N. "AFRL Neutral Density Support to HASDM," presented as paper AIAA-2002-4891 at the AIAA/AAS Astrodynamics Specialist Conference and Exhibit, Monterey, California, August 5–8, 2002.

[28] BOWMAN, B. R. "HASDM/Sapphire Dragon Projects," Atmosphere Neutral Density and Solar Indices Workshop, Colorado Springs, Colorado, October 12–13, 2005.

[29] FULLER-ROWELL, T. J. and REES, D. "A Three-Dimensional, Time-Dependent, Global Model of the Thermosphere," *Journal of Atmospheric Science,* Volume 37, 1980, pp. 2545–2567.

[30] FULLER-ROWELL, T. J. and REES, D. "Derivation of a Conservative Equation for Mean Molecular Weight for a Two Constituent Gas Within a Three-Dimensional, Time-Dependent Model of the Thermosphere," *Planetary Space Sciences,* Volume 31, 1983, pp. 1209–1222.

[31] QUEGAN, S., BAILEY, G. J., MOFFETT, R. J., HEELIS, R. A., FULLER-ROWELL, T. J., REES, D., and SPIRO, J. "A Theoretical Study of the Distribution of Ionization in the High-Latitude Ionosphere and Plasmasphere: First Results on the Mid-Latitude Trough and the Light Ion Trough," *Atmosphere Terrestrial Physics,* Volume 44, 1982, pp. 619–640.

[32] FULLER-ROWELL, T. J., REES, D., QUEGAN, S., MOFFETT, R. J., CODRESCU, M. V., and MILLWARD, G. H. "A Coupled Thermosphere-Ionosphere Model (CTIM)," *Solar-Terrestrial Energy Program: Handbook of Ionospheric Models,* Scientific Committee on Solar Terrestrial Physics (SCOSTEP), August, 1996, pp. 217–238.

[33] MINTER, C. F. *Thermospheric Composition Forecasting Using Kalman Filtering Techniques,* Ph.D. Dissertation, University of Colorado, August 2002.

[34] SILVEY, S. D. "Multicollinearity and Imprecise Estimation," *Technometrics,* Volume 11, October, 1969, pp. 539–552.

[35] GOLDSTEIN, M. "The Poorly Conditioned Data on Multiple Regression Procedures," *British Journal of Mathematical Psychology,* Volume 31, 1978, pp. 102–105.

[36] MARCOS, F. A. "Analysis of Neutral Density from Drag, Accelerometers & Remote Sensing," Atmosphere Neutral Density and Solar Indices Workshop, Colorado Springs, Colorado, October 12–13, 2005.

[37] RISHBETH, H. and GARRIOTT, O. K. *Introduction to Ionospheric Physics,* Academic Press, London, 1969.

[38] SCHUNK, R. W. and NAGY, A. F. *Ionospheres: Physics, Plasma Physics, and Chemistry,* Cambridge University Press, New York, 2000, pp. 216–220 and 344–345.

[39] SOJKA, J. J. and SCHUNK, R. W. "A Theoretical Study of the High Latitude *F* Region's Response to Magnetospheric Storm Inputs," *Journal of Geophysical Research,* Volume 88, 1983, pp. 2112–2122.

[40] PRÖLSS, G. W., BRACE, L. H., MAYR, H. G., CARIGNAN, G. R., KILLEEN, T. L., and KLOBUCHAR, J. A. "Ionospheric Storm Effects at Subauroral Latitudes: A Case Study," *Journal of Geophysical Research,* Volume 96, 1991, pp. 1275–1288.

[41] FOSTER, J. C., HOLT, J. M., MUSGROVE, R. G., EVANS, D. S. "Ionospheric Convection Associated with Discrete Levels of Particle Precipitation," *Geophysical Research Letters,* Volume 13, 1986, pp. 656–659.

[42] FULLER-ROWELL, T. J. and EVANS, D. S. "Height-Integrated Pedersen and Hall Conductivity Patterns Inferred from the TIROS-NOAA Satellite Data," *Journal of Geophysical Research,* Volume 92, 1987, pp. 7606–.

[43] FULLER-ROWELL, T. J., MATSUO, T., CODRESCU, M. V., and MARCOS, F. A. "Modeling Thermospheric Neutral Density Waves and Holes in Response to High-Latitude Forcing," *Advances in Space Research,* Volume 24, 1999, pp. 1447–1458.

[44] McCOY, R. and THONNARD, S. "Special Sensor Ultraviolet Limb Imager," Brochure of Praxis Inc., Naval Research Laboratory, Washington, D. C., 1997.

[45] PAXTON, L. J., MENG, C.-I., FOUNTAIN, G. H., OGORZALEK, B. S., DARLINGTON, E. H., GARY, S. A., GOLDSTEN, J. O., KUSNIERKIEWICZ, D. Y., LEE, S. C., LINSTROM, L. A., MAYNARD, J. J., PEACOCK, K., PERSONS, D. F., SMITH, B. E., STRICKLAND, D. J.,

and DANIELL, R. E. "SSUSI: Horizon-to-Horizon and Limb-Viewing Spectrographic Imager for Remote Sensing of Environmental Parameters," *Ultraviolet Technology IV, SPIE,* Vol. 1764, 1992, pp. 161–175.

[46] EVANS, J. S., STRICKLAND, D. J., and WRIGHT, K. C. "SSUSI Dayside F_2-Region Algorithm Language-Independent Description," Technical Report No. 19, Version 3, Applied Physics Laboratory, Laurel, Maryland, April 1995.

[47] STRICKLAND, D. J., EVANS, J. S., and PAXTON, L. J. "Satellite Remote Sensing of Thermospheric O/N_2 and Solar EUV: 1. Theory," *Journal of Geophysical Research,* Volume 88, 1983, pp. 2112–2122.

[48] HOBSON, E. W. *The Theory of Spherical and Ellipsoidal Harmonics,* Chelsea Publishing, New York, 1931, reprinted in 1965.

[49] CICCI, D. A. and TAPLEY, B. D. "Optimal Solutions of Unobservable Orbit Determination Problems," *Celestial Mechanics,* Volume 44, 1988, pp. 339–369.

[50] MONTGOMERY, D. C. and RUNGER, G. C. *Applied Statistics and Probability for Engineers,* John Wiley & Sons, Inc., New York, 1994, pp. 175–178, A-6, and A-7.